Food Hydrocolloids 160 (2025) 110783

Contents lists available at ScienceDirect

Food Hydrocolloids

journal homepage: www.elsevier.com/locate/foodhyd

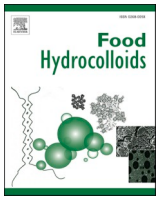

# Rubisco at interfaces I: Conformational flexibility enhances air-water interface and foam stabilization

Xingfa Ma, Thomas van Polen, Mehdi Habibi, Jasper Landman, Leonard M.C. Sagis, Penghui Shen *

*Laboratory of Physics and Physical Chemistry of Foods, Wageningen University, Bornse Weilanden 9, 6708 WG, Wageningen, the Netherlands*

ARTICLE INFO

*Keywords:*
Rubisco
Molecular structure
Air-water interface
Interfacial rheology
Interfacial structure
Foaming properties

ABSTRACT

Rubisco exists in all green leaves and is the most abundant protein species on earth. Extraction methods can affect the molecular conformation of Rubisco, while its influence in the behavior of Rubisco at the air-water interface and foam stabilization is largely unknown. This work focuses on elucidating the role of the Rubisco molecular structure in stabilizing the air-water interface and the multiphase system of foam. Rubisco was extracted from spinach using ultrafiltration (RU) and acid precipitation-alkaline redispersion (RA), respectively. Protein molecular properties were evaluated using SDS-PAGE, DSC, fluorescence spectrometry, and size and zeta-potential measurements. Surface adsorption behavior was measured in the millisecond and longtime regime. Surface mechanical properties were assessed with large amplitude oscillatory dilatation (LAOD) and large amplitude oscillatory shear (LAOS), and LAOD results were analyzed by stress decomposition. Interfacial structures were characterized by imaging Langmuir-Blodgett films with atomic force microscopy. Protein foaming properties were evaluated by whipping. We found that RU was primarily native and more flexible than RA, which was fully denatured and aggregated. Consequently, RU diffused faster to air-water interface (576 ms) than RA (926 ms), and formed stiffer soft solid-like air-water interfaces ($G_i$' = 56.7 mN/m; $E_d$' = 98.2 mN/m) than RA ($G_i$' = 39.6 mN/m; $E_d$' = 84.3 mN/m). RU also formed denser and thicker surfaces with higher network connectivity than RA. These advantages endow RU with much higher foam stability (152 min half-life time) than RA (94 min). Our study reveals a clear relationship between the molecular conformation of Rubisco and its air-water interface and foam stabilization properties. It might also guide the development of improved extraction/treatment methods to obtain ideal molecular structures of proteins for foam stabilization.

## 1. Introduction

Rubisco, an abbreviation of ribulose-1,5-bisphosphate carboxylase/oxygenase, is a key enzyme in photosynthetic organisms to fix carbon dioxide from the atmosphere into organic carbon (Pearce & Brunke, 2023). This protein occupies 50% of the whole soluble protein in green leaves and is estimated to constitute 0.2% of the world's protein (Ellis, 1979). Thereby, it is deemed as the most abundant protein species on earth. At a molecular level, Rubisco is a compact and nearly spherical protein molecule with a molecular weight of around 560 kDa and consists of eight large subunits (around 50 kDa) and eight small subunits (around 15 kDa), which are combined through hydrophobic interactions (Barbeau & Kinsella, 1988). The large subunits are arranged symmetrically in a tetrameric toroid, while the small subunits are attached at the ends of the large subunit core (Andersson & Backlund, 2008).

Beyond acting as a photosynthetic enzyme, Rubisco has been also identified as a novel food functional material (e.g., a foamer and an emulsifier) for decades, which could be at the same time an ideal protein source for human and animal consumption due to its favorable nutritional values, bioactivities and non-allergenicity (Grácio, Oliveira, Lima, & Ferreira, 2023; Jeurink & Savelkoul, 2006). In 1985, Sheen and Sheen (1985) demonstrated that Rubisco from Tobacco leaves had higher foamability and foam stability than egg white and soy protein isolate. Later on, Rubisco from more types of leaves (e.g. sugar beet (Martin, Castellani, de Jong, Bovetto, & Schmitt, 2019), kale (Nynäs, Newson, Langton, Wouters, & Johansson, 2023), radish (Rawiwan & Quek, 2024), cabbage (Rawiwan et al., 2024), water lentil (Muller, Bernier, & Bazinet, 2023), and alfalfa (Lamsal, Koegel, & Gunasekaran, 2007)) also displayed high foaming properties. Although Rubisco is gaining increasing attention as a good foamer, few studies investigated its

* Corresponding author.
*E-mail address:* Bittersweet_Sph@163.com (P. Shen).

https://doi.org/10.1016/j.foodhyd.2024.110783
Received 11 July 2024; Received in revised form 20 September 2024; Accepted 24 October 2024
Available online 28 October 2024

behavior at the air-water interface and in foam stabilization. According to Nynäs et al. (2023), crude Rubisco extract-stabilized air-water interfaces displayed high interfacial stiffness, which was comparable to egg white protein-stabilized ones. But the origin of the high interfacial stiffness and how the crude Rubisco extract stabilized foams were not investigated. Thus, the underlying mechanisms by which Rubisco stabilizes air-water interface and foam are still largely unknown.

Interfacial properties of proteins including interfacial adsorption, structure rearrangement, and in-plane interaction at the interface (Hinderink et al., 2022; Tang, 2017), are largely determined by the molecular structure of proteins (Tang, 2017). Therefore, to unravel the foam stabilization mechanism of Rubisco, it is essential to understand the role of its molecular structure in air-water interface stabilization. One can do this by tuning the molecular structure of Rubisco by employing different treatments (e.g. pH, temperature, sonication, pressure and ionic strength) and studying their influence on the interfacial behavior of Rubisco. Adjusting pH is the easiest method for altering the protein conformational structure, which can largely change the electrostatic repulsive interactions between protein subunits, causing substantial structural unfolding and reassembly of protein molecules (Kristinsson & Hultin, 2003; Seckler & Jaenicke, 1992; Zhou & Pang, 2018).

The first step toward studying the interfacial properties of this protein is the extraction of Rubisco while retaining nativity and functionalities (e.g. solubility). In most studies, Rubisco was extracted from leaves due to its relatively high content in leaves. In general, fresh leaf juice is first obtained by blending or extrusion of leaves, followed by the processes of removing the chlorophyll and insoluble leaf residues (Martin et al., 2019). The Rubisco-rich juice is then further purified by ultrafiltration, chromatography separation, or acid precipitation (Kobbi et al., 2017; Lamsal et al., 2007; Martin et al., 2019). Ultrafiltration and acid precipitation give much higher yields and are much less time-consuming compared to the chromatography separation method, thus they are more scalable for the production of Rubisco (Barta, Carmo-Silva, & Salvucci, 2011; Buyel, Twyman, & Fischer, 2015; Heppner & Livney, 2023; Kobbi et al., 2017; Venkataraman, Rajendran, Kumar, Vo, & Vaidyanathan, 2022). Ultrafiltration is the most commonly used method in purifying Rubisco, and it can largely keep the nativity of Rubisco (Zhang, Grimi, Jaffrin, Ding, & Tang, 2017). But the obtained Rubisco extracts often display relatively low purity (~50%) (Zhang et al., 2017) compared to those purified by chromatography separation and acid precipitation (~90%) (Kobbi et al., 2017). Although acid precipitation can produce Rubisco extract with rather high purity, researchers often found that the extracts were difficult to redisperse in water due to the severe aggregation of Rubisco molecules (Kobbi et al., 2017; Lamsal et al., 2007). Thus, Rubisco extracted by this method cannot function well in foam stabilization (Lamsal et al., 2007). Adjusting pH is a powerful tool to unfold protein structures, and it is expected to dissolve insoluble Rubisco aggregates when the pH is high enough (e.g. pH 12) as this often works for other proteins (Jiang, Xiong, & Chen, 2010). The unfolding/reassembly effect of pH adjusting on protein molecules is expected to alter the molecular conformation of Rubisco.

To gain insights on how the alteration of the molecular conformation of Rubisco influences its air-water interface and foam stabilization behavior, we applied two extraction methods –ultrafiltration and acid precipitation-alkaline redispersion–to produce Rubisco proteins (RU and RA) with different molecular conformations. The molecular properties of RU and RA were characterized by SDS-PAGE, zetasizer, and surface hydrophobicity measurements. Their behavior at the air-water interface was systematically studied, including adsorption in both short-time (milliseconds) and long-time (hours) scales, interfacial shear and dilatational rheology with both LAOS and LAOD tests, and interfacial structures evaluated by ellipsometry and AFM. The foaming properties of RU and RA were determined and elucidated with the molecular and interfacial properties of RU and RA. This study helps to comprehensively understand the link between molecular conformation and interfacial and foaming properties of rubisco proteins, which might be also useful to guide the proper choice of extraction/treatment methods for other proteins to obtain ideal molecular structures for foam stabilization.

## 2. Experimental section

### 2.1. Materials

Spinach (Spinacia oleracea) was purchased from a local supermarket (Jumbo, Wageningen, The Netherlands). All chemicals (Sigma-Aldrich, USA) and the materials for SDS-PAGE (Invitrogen Novex, ThermoFisher Scientific, USA) were used as received. Ultrapure water (MilliQ Purelab Ultra, Germany) was used for all experiments unless indicated elsewhere.

### 2.2. Sample preparations

#### 2.2.1. Protein extraction process

Fresh spinach was blended into a slurry after mixing with phosphate buffer (20 mM, pH 7) at a 2:1 (w/v) ratio. The slurry was then filtrated through cheesecloth to obtain crude juice. Polyvinylpolypyrrolidone (PVPP) was added to the juice at 30 g/L concentration and heated at 50 °C for 1 h to remove chlorophyll. This mixture was centrifuged at 17000 g (20 °C, 20 min), and the supernatant was collected and subjected to Rubisco purification with either ultrafiltration or acid precipitation. In ultrafiltration, the supernatant was filtrated through a 100 kDa membrane on a Vivaflow® 50R 200 System (Sartorius, Germany) under a pressure of 2.5 bar until 90% of the initial volume was reduced. The retentate was continuously exchanged with two volume folds of phosphate buffer (20 mM, pH 7) and further dialyzed over 12–14 kDa membrane against deionized water for two days with at least three times water exchange. In acid precipitation, the supernatant was adjusted to pH 3.5 with 1 M HCl for 30 min and centrifuged at 17000 g (20 °C, 20 min) to obtain a pellet. This pellet was mixed with deionized water at a 1:6 (w/w) ratio and adjusted to pH 12 with 1 M NaOH to fully dissolve the pellet and dialyzed with the same procedure as mentioned above. After dialysis, the samples were freeze-dried and kept at 4 °C until further use.

#### 2.2.2. Protein solubility measurement

Rubisco dispersions were prepared at 1.0 wt% at 20 mM pH 7.0 phosphate buffer under stirring for 1 h and kept at 4 °C overnight for protein hydration. Before measurement, the protein dispersions were passed through a 0.45 μm filter to remove any insoluble materials, followed by overnight drying of the protein samples in an oven at 60 °C. A Flash EA 1112 Series Dumas (Interscience, The Netherlands) was used to measure the nitrogen content of the dried protein samples. A nitrogen conversion factor of 5.7 was used to calculate the protein content.

#### 2.2.3. Solution preparations

Rubisco dispersions were prepared at 0.1 wt% soluble protein concentration. Briefly, protein extracts were dissolved in 20 mM pH 7.0 phosphate buffer and stirred for 1 h at room temperature before keeping at 4 °C overnight for complete protein hydration. Afterward, the protein dispersions were passed through a 0.22 μm filter to remove any insoluble materials before further analysis.

### 2.3. Determination of protein compositions by SDS-PAGE

Rubisco extracts (RU and RA) were dispersed in water at 0.1 wt% extract concentration, and then 45 μL of the protein dispersion was mixed with 7 μL of NuPAGE LDS sample buffer and 6 μL of water (for non-reducing conditions) or NuPAGE reducing agents (for reducing conditions). These mixtures were heated at 70 °C for 10 min, and

subsequently, 10 μL of protein markers with a molecular weight of 10–200 kDa and 15 μL of sample mixtures were loaded on a 4–12 w/w% BisTris gel. Electrophoresis was performed in a XCell Surelock Mini-Cell for 30 min at 200 V. Finally, the gel was stained with SimplyBlue SafeStain, destained with MiliQ water and scanned using a GS900 gel scanner (Biorad, USA).

### 2.4. Characterization of protein denaturation properties by DSC

Differential scanning calorimetry (DSC) (TA Instruments, USA) was used to evaluate the nativity of Rubisco protein extracts according to our previous study (Shen, Peng, Sagis, & Landman, 2023). Briefly, 50 μL of 10 wt% Rubisco extracts was injected into a stainless-steel high-volume pan. Samples were initially equilibrated at 20 °C for 5 min, followed by a temperature ramp to 140 °C at a 5 °C/min rate and a subsequent cooling phase back to 20 °C at a 10 °C/min rate. All measurements were performed in triplicates, and an empty pan was used as a reference.

### 2.5. Determination of surface hydrophobicity

The protein surface hydrophobicity was measured by a fluorescence spectrometer (Shimadzu RF 6000 Fluorometer) with 8-anilino-1-napthalenesulfonic acid ammonium salt (ANSA) as a fluorescence probe. Protein stock dispersions were prepared at a concentration of 0.1 wt% in 20 mM phosphate buffer (pH7) and subsequently diluted to a concentration from 0.002 wt% to 0.01 wt% using 20 mM phosphate buffer. Aliquots of 25 μL of 8 mM ANS solutions were added to 4 mL of protein solutions and a 1-h reaction time was allowed before further measurement. The fluorescence intensity was measured at an excitation and emission wavelength of 390 nm and 470 nm, respectively. The buffer with only ANS was involved as a blank. The surface hydrophobicity was calculated as the slope of the linear regression of fluorescence intensity as a function of protein concentration ($R^2 = 0.99$).

### 2.6. Particle size and zeta potential

The particle size and zeta potential of 0.1 wt% Rubisco extracts were measured by a Zetasizer Nano ZS (Malvern Instruments, UK) at 20 °C using dynamic light scattering and microelectrophoresis, respectively. The refractive indices of protein and continuous phase were set to 1.450 and 1.330, respectively.

### 2.7. Adsorption behavior at air-water interface

The air-water adsorption behavior of Rubisco extracts was measured at both short-time (100 ms-3 s) and long-time (1–10800 s) scales by a bubble pressure tensiometer (BPT) and automatic drop tensiometer (ADT), respectively. In BPT measurement, air bubbles were continuously generated from a capillary into 15 mL protein dispersions at different frequencies. The surface tension ($\gamma_s$) was then calculated from the Young-Laplace equation assuming a spherical shape of the air bubble: $\gamma_s = (P_{max}\text{-}P_0)*r/2$, where $P_{max}$, $P_0$, and r are the maximum internal pressure, the hydrostatic pressure, and the capillary radius, respectively. In the ADT measurements, a rising bubble of 12 $mm^2$ was generated at the tip of a J-shape needle and equilibrated in the 0.1 wt% rubisco protein dispersions for 3 h. The surface tension of the air bubble was calculated by the in-built software by fitting the bubble profiles to the Young-Laplace equation. Surface pressure (Π) was calculated as $\Pi = \gamma_w - \gamma_s$, where $\gamma_w$ is the surface tension of a clean air-water interface and $\gamma_s$ is the surface tension in real-time.

### 2.8. Surface rheological properties

#### 2.8.1. Interfacial shear rheology

The air-water interfaces formed by Rubisco were subjected to shear deformation using a stress-controlled MCR 302e rheometer (Anton Paar, Graz, Austria) with a double-wall ring (DWR) geometry. Briefly, aliquots of 15 ml of 0.1 wt% protein dispersions were transferred into a Teflon double wall trough, and the DWR was positioned at the air-water interface. Time sweeps were applied during adsorption at 0.1% strain and 0.1 Hz frequency for 3 h. After that, frequency sweeps were performed at a frequency increasing from 0.01 Hz to 10 Hz with a fixed strain of 1%, followed by strain sweeps conducted with a strain increasing from 0.01% to 100% at a fixed frequency of 0.1 Hz. The data of the frequency sweeps were fitted with a power law equation, $G_i' = \omega^n$, where $G_i'$ is the interfacial shear storage modulus, and ω is the frequency. The results from strain sweeps were used to construct Lissajous plots by plotting stress against strain. All experiments were performed in triplicate at 20 °C.

The energy dissipation ratio of each Lissajous plot from 0.1% to 100% of the strain was calculated from the raw oscillation data according to Ewoldt, Hosoi, and McKinley (2008):

$$\Phi = \frac{\pi \gamma G_i''}{4\sigma_{max}} \quad (1)$$

where γ is the applied strain of the oscillation cycle, $G_i''$ is the interfacial shear loss modulus, and $\sigma_{max}$ is the maximum shear stress.

#### 2.8.2. Interfacial dilatational rheology

Interfacial dilatational rheology was applied during or after protein adsorption for 3 h. During the adsorption, time sweeps were performed at 3% deformation amplitude and at 0.02 Hz frequency. After the adsorption, frequency sweeps were conducted with frequency increasing from 0.005 Hz to 0.1 Hz at a fixed amplitude of 3%. The frequency data were again fitted with a power law model, $E_d' = \omega^n$, where $E_d'$ is the elastic dilatational modulus, and ω is the frequency. The air-water interfaces were then subjected to amplitude sweeps with amplitude increasing from 1 to 50% at a fixed frequency of 0.02 Hz. These experiments were performed in at least triplicate at 20 °C.

The rheological data from amplitude sweeps were analyzed by Lissajous plots according to Sagis and Fischer (2014). Briefly, the Lissajous plots were constructed by plotting surface pressure against deformation ($(A\text{-}A_0)/A_0$), where A is the area of the air bubble in real-time and $A_0$ is the area of the air bubble in the non-deformed state. The middle three cycles from five oscillation cycles were used to construct the Lissajous plots. The Lissajous plots were further analyzed by a general stress decomposition (GSD) method to separate the contributions from odd harmonics and even harmonics (de Groot, Yang, & Sagis, 2023).

### 2.9. Air-water interfacial microstructure

#### 2.9.1. Preparation of Langmuir-Blodgett films and AFM imaging

Langmuir-Blodgett (LB) films were prepared using a Langmuir trough (KSV NIMA/Biolin Scientific Oy, Finland) according to our previous study (Yang et al., 2021). Briefly, the trough was filled with ~200 ml of 20 mM pH 7.0 phosphate buffer, and subsequently, a freshly cleaved mica sheet (Highest Grade V1 Mica, Ted Pella, USA) was immersed into the buffer. Afterward, 200 μL of 0.1 wt% protein dispersions were injected at the bottom of the trough. After 3 h of adsorption, the Teflon barriers were moved at a speed of 5 mm/min to compress the air-water interface to a surface pressure of 10 mN/m or 25 mN/m, with continuous recording of surface pressure by a Wilhelmy plate (platinum, perimeter 20 mm, height 10 mm). Upon reaching the target surface pressure, the mica sheet was lifted at a speed of 1 mm/min, while keeping the surface pressure constant by moving the Teflon barriers. Duplicate films from each surface pressure were prepared and dried in a desiccator for at least 2 days.

The prepared LB films were imaged by using an atomic force microscope (AFM) (NanoWizard® 4XP NanoScience, Bruker Nano GmbH, Germany). The AFM images were captured using a PeakForce Tapping mode connected with a PEAKFORCE-HIRS-F-A cantilever (Bruker Nano

GmbH, Germany) with a tip radius of 1 nm and normal spring constant of 0.42 N/m. These LB films were scanned over 2 × 2 $\mu m^2$ and 0.35 × 0.35 $\mu m^2$ in a lateral resolution of 512 × 512 $pixels^2$ and at a line rate of 1.7 Hz. The resultant images were analyzed using JPK data processing software (Bruker Nano GmbH, Germany).

The AFM images were further quantitatively analyzed by conducting protein network analysis using the Angiotool 64 software (National Cancer Institute, National Institute of Health, Maryland, USA) and pair correlation function using the ImageJ software. The protein network analysis was performed according to previous studies (Bernklau, Lucas, Jekle, & Becker, 2016; Zudaire, Gambardella, Kurcz, & Vermeren, 2011). Briefly, the parameters, such as vessel area, junction density, average vessel length, lacunarity, branching rate, and end-point rate were calculated by the Angiotool 64 software to characterize the protein network. Regarding the pair correlation function (g(r)), it indicates the probability of finding a particle at a given distance to a reference point. When g(r) is equal to 1, it suggests a uniform distribution of proteins at the interface, while the value of g(r) larger than 1 indicates the occurrence of protein aggregation (Binder & Simpson, 2013). In this study, we take the distance where g(r) reduces to 1 as protein domain size and the maxima of g(r) as an indicator of the heterogeneity of the film.

#### 2.9.2. Interfacial thickness

The interfacial thickness was measured with an imaging nulling ellipsometer EP4 (Accurion, Germany) according to our previous study (Shen, Peng, et al., 2023). Briefly, 10 mL of samples was injected into a Petri dish (60 mm in diameter). After 3 h of adsorption, the air-water interfacial thickness was measured at a wavelength from 499.8 nm to 793.8 nm over two zones. The output was processed by an EP4Model v.3.6.1. software. All measurements were performed at least in triplicate at room temperature.

### 2.10. Foaming properties

Foamability and foam stability were evaluated by measuring foam overrun (%) and foam half-life time (min) based on our previous study with minor modifications (Shen, Peng, et al., 2023). For the foamability measurement, aliquots of 10 ml of samples were injected into a cylindrical container (34 mm diameter) and whipped using a frother (Aerolatte, UK) at 2000 rpm for 2 min. The initial foam height after whipping was measured by a ruler and used to calculate the foam overrun (foam volume/initial liquid volume × 100%). For the foam stability measurement, the foam after whipping was transferred to a glass cylinder, and the foam volume was continuously monitored. The time that half the volume of the foam decayed, also called foam half-life time, was used to evaluate the foam stability. All measurements were performed at least in triplicate at room temperature.

### 2.11. Statistical analysis

One-way analysis of variance (ANOVA) of the data was conducted by OriginPro 2021. The means comparison among samples was conducted by the Ducan test using a significant level of 0.05.

## 3. Results and discussion

### 3.1. Physiochemical properties of rubisco extracts

Rubisco extracts by ultrafiltration (RU) and acid precipitation-alkaline redispersion (RA) have high protein contents of 78.6% and 90.7%, respectively. RU shows a high protein solubility (95.8%) in 20 mM pH 7.0 phosphate buffer due to its mild extraction process. Surprisingly, the extensively extracted Rubisco protein RA also shows high protein solubility (91.7%), which was previously reported to be poorly soluble, such as acid-precipitated alfalfa leaf proteins (20–40%) (Lamsal et al., 2007). In our case, the high protein solubility of Rubisco extracted from acid precipitation might be attributed to the high pH processing during extraction (pH 12), which can largely disassociate protein precipitates by strong electric repulsion and extensively change the molecular structure of Rubisco (Jiang et al., 2010). This may have favored the redispersion of RA at neutral pH.

Electrophoresis (SDS-PAGE) was used to study the protein composition in RU and RA (Fig. 1) in both non-reducing and reducing conditions. The non-reducing conditions can disassemble protein subunits by disrupting the hydrophobic interactions by the denaturant SDS which would bring a large amount of negative charge and cause high electrostatic repulsion, and the reducing conditions can further disrupt the disulfide bonds between subunits by another denaturant, DTT. Under non-reducing conditions, the SDS-PAGE patterns of RU showed two main bands at molecular weights (MW) around 50 kDa and 15 kDa that correspond to the large and small subunits of Rubisco, respectively (Barbeau et al., 1988; Douillard & De Mathan, 1994; Martin, Nieuwland, & de Jong, 2014). In contrast, the bands of RA are mainly distributed at MW higher than 100 kDa, which indicates that RA primarily comprises large aggregates. Under reducing conditions, the bands of RA at large MW largely diminished and reduced to the large and small subunits of Rubisco at around 50 kDa and 15 kDa, respectively. This suggests that the protein subunits in RA are mainly linked by disulfide bonds. RU shows overall similar gel patterns under non-reducing and reducing conditions with a minor band at MW around 120 kDa in non-reducing conditions disappearing in reducing conditions, indicating the minor presence of disulfide bonds in RU. Hence, it can be concluded that the molecular structure of RU is mainly stabilized by hydrophobic interactions, while RA's structure is mainly stabilized by disulfide bonds, and is also in a more aggregated state. The richness of disulfide bonds in RA is ascribed to the extreme pH condition during extraction (pH 12), at which the protein structure will be highly unfolded due to strong electrostatic repulsion between polypeptide chains. Thus, the buried -SH were exposed and meanwhile became active due to deprotonation (loss of $H^+$) (Poole, 2015; R. Y. H. Tan, Lee, Pichika, Cheng, & Lam, 2022),

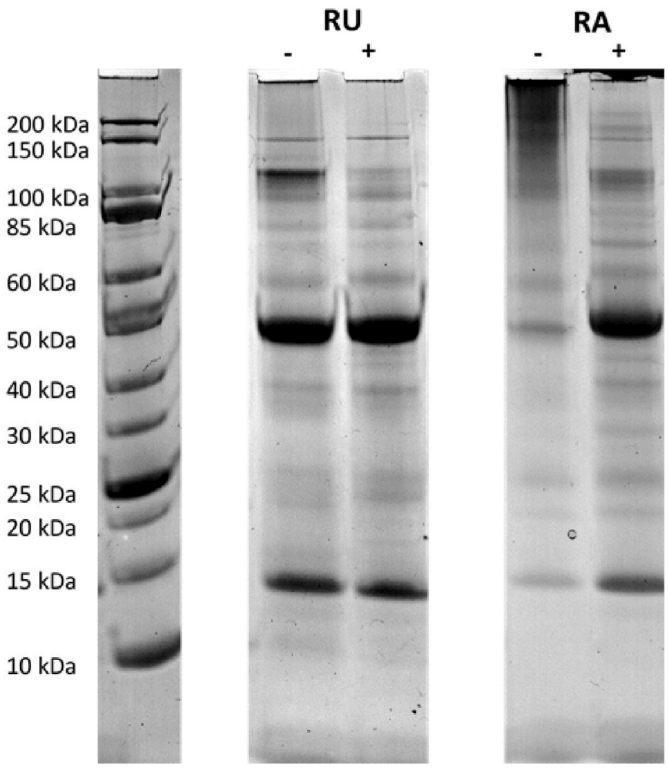


**Fig. 1.** SDS-PAGE profiles of Rubisco extracts (RU and RA) under non-reducing (−) and reducing (+) conditions containing marker (indicated on the left).

leading to the formation of disulfide bonds (S-S) between protein molecules and promoting protein aggregation (Moreno, García-Murria, & Marín-Navarro, 2008). The dominant intra/intermolecular force of disulfide bonds in RA is expected to cause higher molecular rigidity of RA than RU.

The particle size distribution and zeta potential of RU and RA in 20 mM pH 7.0 phosphate buffer are shown in Fig. 2. RU and RA clearly show monomodal distributions with peaks at 13.1 nm and 20.5 nm, respectively, demonstrating that RA has a larger particle size than RU due to aggregation and possibly reassembly of the molecular structure after the high pH processing, and the decrease of pH to neutral. This phenomenon is in line with the existence of large aggregates of RA in its SDS-PAGE patterns (Fig. 1). RU shows a surface charge of −15 (±1.2) mv, which has a lower value than RA (−20 ± 0.9 mv) (Fig. 2B). The discrepancy in surface charges between RU and RA might be attributed to the rearrangement of polar groups on the surface of Rubisco molecules during pH shifting (Parsegian & Rand, 2019; Verruto, Le, & Kilpatrick, 2009). According to differential scanning calorimetry (DSC) measurement, RU has a denaturation temperature at 64.05 ± 0.03 °C with denaturation enthalpy of 5.19 (±0.13) J/g protein, while RA has no apparent endothermal peaks. These phenomena clearly demonstrate that RU is predominantly in a native state, while RA was completely denatured by the high pH treatment. As shown in Fig. 2C, RA shows higher surface hydrophobicity than RU due to its extensive structure rearrangement during the pH shifting progress that could cause the exposure of interior hydrophobic groups (Ge et al., 2021). Overall, RU is mostly in a native state with small particle sizes. Conversely, RA is fully denatured and has a considerable fraction of larger protein aggregates with a higher negative charge and surface hydrophobicity than RU.

### 3.2. Adsorption behavior of rubisco proteins at the air-water interface

The adsorption behavior of RU and RA at the air-water interface was characterized within the sub-second regime (100 ms-3 s) by a bubble pressure tensiometer (BPT) and long-time regime (1–10800 s) by an automatic drop tensiometer (ADT). Fig. 3A shows that for RU surface pressure started to increase at around 576 ms, while the increase of surface pressure in RA occurred at around 926 ms. RU adsorbed more rapidly to the interface than RA, in spite of the higher exposed hydrophobicity of RA. This may in part be due to the smaller particle size of RU (13.1 nm) compared to RA (20.5 nm), allowing for faster diffusion of RU towards the interface. In our previous studies, napin (Shen, Yang, Nikiforidis, Mocking-Bode, & Sagis, 2023), whey protein (Buchmann et al., 2019), and lentil protein (Shen, Peng, et al., 2023) had an adsorption lag time of 83 ms, 130 ms, and 300 ms, respectively. These proteins had a smaller particle size than RU and RA, around 3.4 nm, 4 nm, and 11.3 nm, respectively. Thus, the particle size seems to play a dominant role in the air-water interfacial adsorption of proteins. The lower charge of RU may in addition lower the energy barrier for adsorption, which may also have contributed to the lower lag time. After 3 h of adsorption, RU increased the surface pressure to 26.2 ± 0.3 mN/m, while RA increased the surface pressure to a lower level of 23.1 ± 0.1 mN/m (Fig. 3B). The differences in the quasi-equilibrium surface pressure might be caused by the differences in the structural arrangement of RU and RA at the interface and the differences in protein-protein in-plane interactions (P. Wierenga & Gruppen, 2010; P. A. Wierenga, Meinders, Egmond, Voragen, & de Jongh, 2003). RA has a more rigid molecular structure maintained by disulfide bonds compared to RU which is maintained by hydrophobic interactions (Fig. 1), and this likely caused a lower extent of structural rearrangement and in-plane interactions of RA, leading to a lower surface pressure.

To monitor the development of the air-water interfacial mechanical properties of RU and RA, interfacial shear time sweeps at a strain of 0.1% and frequency of 0.1 Hz were performed during 3 h of adsorption, as shown in Fig. 3C. The moduli $G_i$' of both RU and RA follow power-law behavior with adsorption time, which is similar to the behavior of the aging of structural glasses (Negi & Osuji, 2010). RU displays a higher exponent (0.35) from the power-law fitting than RA (0.18) (Table S1), indicating faster structural rearrangement of RU at the interface. For both RU and RA, their storage moduli ($G_i$') are higher than the loss moduli ($G_i$'') after about 60 s of adsorption, suggesting a fast formation of soft solid-like interfaces. The $G_i$' of RA is higher than that of RU during roughly the first 1000 s, suggesting that RA can form a stiffer interface than RU in the early stages of adsorption. This phenomenon could be the result of the higher surface hydrophobicity of RU (Fig. 2C), which can promote protein-protein in-plane interactions through hydrophobic interactions, after protein adsorption to the interface. The faster growth of $G_i$' of RU leads to a crossover with that of RA at around 1000 s, after which RU has a higher $G_i$', finally reaching a value of 52.2 (±2.6) mN/m after 3 h of adsorption. This is significantly higher than the value of RA (36.4 ± 2.7 mN/m). The higher increase rate of $G_i$' of RU is ascribed to its more flexible molecular conformation compared to RA, which facilitates the rearrangement of protein structures at the interface and promotes the formation of stronger and denser interfacial structures at the later adsorption stages (Martin, Grolle, Bos, Stuart, & van Vliet, 2002).

The interfaces stabilized by RU and RA were also subjected to time sweeps during 3 h of adsorption using dilatational rheology. Similarly, RA formed a slightly stronger interface than RU in the initial 1000s, and afterward, the moduli $E_d$' of RU and RA again followed power-law behavior with the adsorption time (Fig. 3D). Just like in interfacial shear, RU had a higher exponent (0.15) than RA (0.08) (Table S1), leading to higher $E_d$', i.e., higher interfacial stiffness of RU than RA after 3 h of adsorption.

### 3.3. Air-water interfacial rheological properties of rubisco proteins after adsorption

#### 3.3.1. Interfacial shear rheology

After 3 h of adsorption, the air-water interfaces were further subjected to frequency sweeps (0.01–10 Hz) at a strain of 1% (Fig. 4A). The

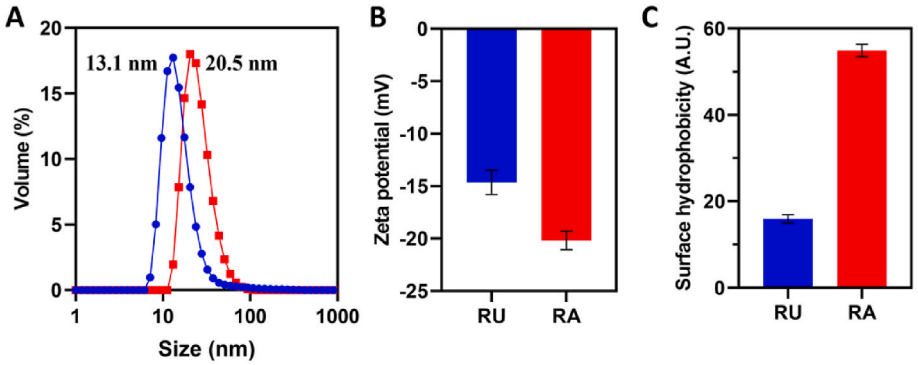


**Fig. 2.** Particle size distribution (A), zeta potential (B), and surface hydrophobicity (C) of 0.1% (w/w) Rubisco (RU and RA) in 20 mM pH 7.0 phosphate buffer.

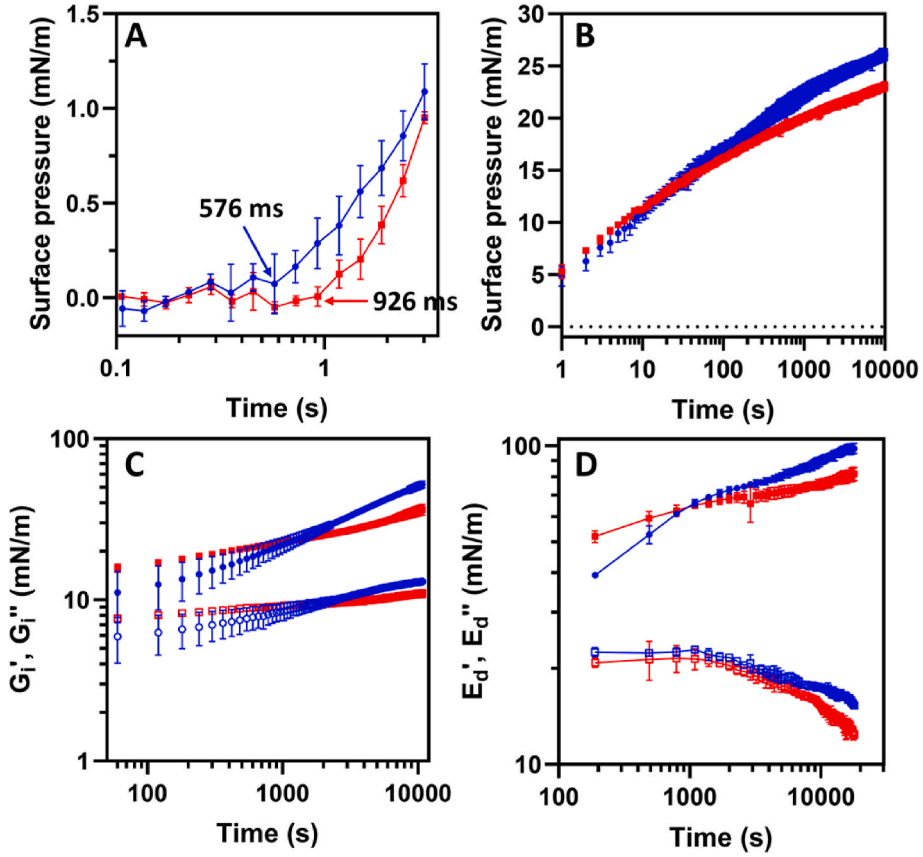


**Fig. 3.** Surface pressure of Rubisco (RU ● and RA ■) as a function of time within the sub-second regime (A) and long-time regime (B). (C) The surface shear storage modulus ($G_i'$) and loss modulus ($G_i''$) of Rubisco (RU ● and RA ■) as a function of time. (D) Interfacial dilatational storage modulus ($E_d'$) and loss modulus ($E_d''$) for Rubisco (RU ● and RA ■) as a function of time. All samples were prepared at a 0.1 wt% concentration in 20 mM pH 7.0 phosphate buffer.

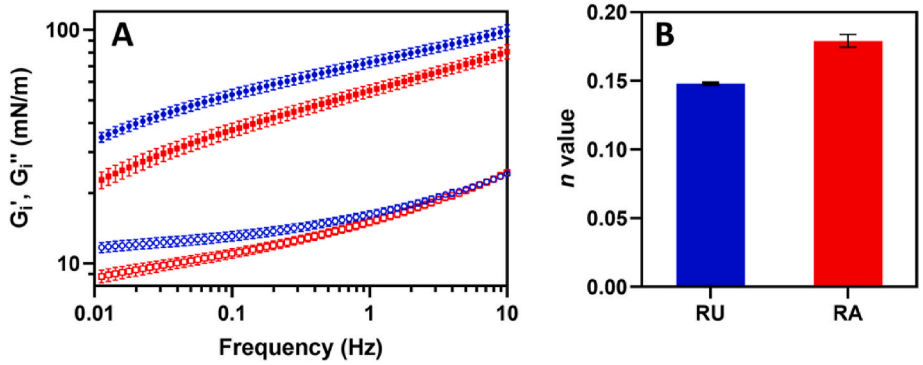


**Fig. 4.** The surface shear storage modulus ($G_i'$) and loss modulus ($G_i''$) of Rubisco (RU ● and RA ■) as a function of frequency (A). (B) The *n* values from power-law fitting ($G_i' \sim \omega^n$) obtained from the surface shear frequency sweep at a fixed strain of 1% for Rubisco proteins (RU and RA). All solutions were prepared at 0.1 wt% in 20 mM pH 7.0 phosphate buffer.

$G_i'$ of both RU and RA is larger than $G_i''$ at all applied frequencies, indicating viscoelastic solid-like behavior for these air-water interfaces in shear. The $G_i'$ of both RU and RA show low dependency on frequency and follow weak power-law behavior (Fig. 4B) (the *n* values obtained from fitting the data with a power law, i.e., $G_i' \sim \omega^n$, were smaller than 0.2). These results suggest that both RU and RA formed soft disordered solid-like air-water interfaces with a wide spectrum of relaxation times.

Subsequently, the interfaces were subject to strain sweeps with strain increasing from 0.1 to 100% at a fixed frequency of 0.1 Hz. The $G_i'$ of RU and RA remain constant until reaching a critical strain, which represents the extent of the linear viscoelastic (LVE) regime. The extent of a LVE regime indicates the stretchability of the air-water interface in response to shear deformation. RA shows a comparable extent of the LVE (1.6 ± 0.2%) to RU (1.5 ± 0.1%), while RU has a higher $G_i'$ of 56.7 (±3.8) mN/m than RA with $G_i'$ of 39.6 (±2.7) mN/m in the LVE. This indicates that the RU-stabilized interface is similarly stretchable in response to shear deformation with the RA-stabilized interface, but it is stiffer. Beyond the LVE, the $G_i'$ of both RU and RA decreases, but $G_i'$ remains higher than

$G_i$'' even at 100% strain, indicating a predominantly elastic behavior of the interfaces formed by both RU and RA in the non-linear viscoelastic (NLVE) regime.

In the calculation of the interfacial shear moduli, only the intensity and phase of the first harmonic of the Fourier transform of the surface stress was used. In the non-linear regime, higher-order harmonics are present in the stress signal. To get more insights into the non-linear behavior of RU and RA in the NLVE regime, we further constructed normalized Lissajous plots (Fig. 5B) with stress decomposition into elastic and viscous contributions. Overall, the Lissajous plots of RU and RA are rather similar in shape in the whole range of shear deformation. At a strain of 0.5% (in LVR), all plots are narrow and elliptical with straight decomposed elastic stress curves, indicating a dominant elastic behavior over viscous behavior. Further increasing the strain from 0.5% to 30%, the Lissajous plots become similarly rhomboidal and wider, where the decomposed elastic component curves are similarly slightly distorted, suggesting a similar degree of disruption of the interfacial structure. At 100% strain, the Lissajous plots of RU and RA show transitions to plastic behavior, while the curve of the elastic component retains a distinctly positive slope, indicating the interfacial structures of RU and RA are disrupted more at large shear strain but still retain some residual elasticity. To quantitatively analyze the Lissajous plots, we calculated the energy dissipation ratio (Φ) based on the method established by Ewoldt et al. (2008). Overall, RU and RA display comparable Φ in the whole shear deformation range. In the LVE regime, the dissipation ratios of RU- and RA-stabilized air-water interfaces were smaller than 0.2, indicating the dominance of elastic behavior. In the NLVR regime (2–100%), the Φ of both RU and RA rapidly increase, finally reaching 0.52 and 0.48 at 100% strain, respectively. Overall, in shear deformation, the RU-stabilized air-water interface is stiffer than the RA-stabilized interface, while they have similar stretchability and comparable non-linear rheological behavior.

### 3.3.2. *Interfacial dilatational rheology*

In the frequency sweeps (Fig. 6A), the elastic moduli ($E_d$') of both interfaces were higher than the viscous moduli ($E_d$''), suggesting the solid-like behavior of these interfaces in dilatation as well. Additionally, the $E_d$' of RU- and RA-stabilized interfaces also follow weak power-law relationships with frequency ($E_d' \sim \omega^n$), and RU and RA showed *n* values of 0.11 and 0.14 (Fig. 6B), respectively, much lower than 0.5. When the *n* value is close to 0.5, the responses of interfaces are mainly determined by the exchange of interfacial stabilizers between bulk and interface (Lucassen & Van Den Tempel, 1972). The low *n* values here indicate the exchange of interfacial stabilizers was not the main mechanism determining the rheological behavior, but other factors might play a role, such as protein-protein in-plane interactions or momentum transfer between bulk and interface (Sagis et al., 2019). The weak power-law behavior and the fact that $E_d''/E_d' < 1$ again indicate the interfaces stabilized by both RU and RA are in a disordered solid-like state. Over the full range of amplitudes applied in the amplitude sweep (Fig. 6C), $E_d$' of RU and RA were larger than their $E_d$''), indicating that the elastic behavior of the interfaces dominates their response to both small and large dilatational deformations. At the small deformation amplitude of 1%, RU has higher $E_d$' (98.2 ± 2.9 mN/m) than RA (84.3 ± 5.3 mN/m), suggesting RU has stronger in-plane interactions at the interface and thus formed a stiffer air-water interface than RA. At a common low deformation amplitude of 3%, the $E_d$' of RU (87.4 ± 1.9 mN/m) and RA (75.2 ± 2.5 mN/m) are significantly higher than many common plant proteins, such as lentil proteins (~62 mN/m) [8], rapeseed proteins (~66 mN/m) [4], pea globulins (~33 mN/m) [23] and mung bean proteins (~53 mN/m) [24], which implies the high potential of Rubisco in stabilizing air-water interface and foams. With increasing deformation amplitude, the $E_d$' of both RU- and RA-stabilized interfaces decreases due to the disruption of the interfacial microstructure. The $E_d$' of the RU-stabilized interface reduces to 31.0 mN/m at 50% deformation amplitude, which is still pronouncedly higher than that of the RA-stabilized interface (23.7 mN/m). This phenomenon implies that the

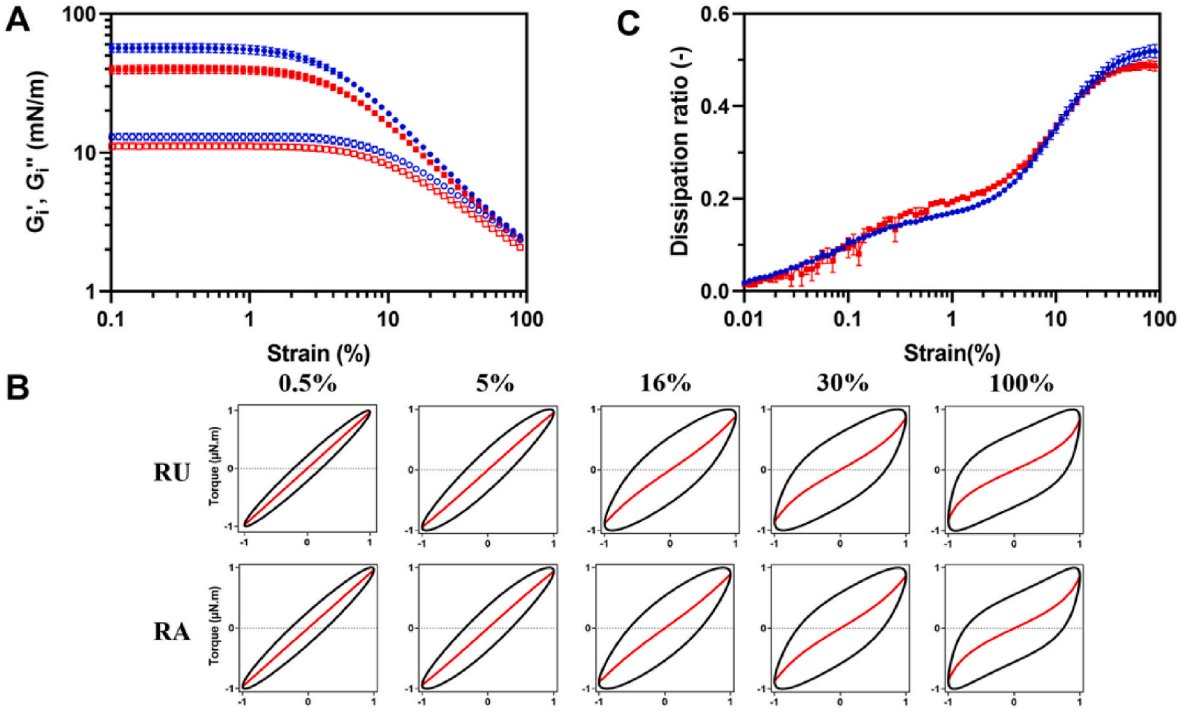


**Fig. 5.** (A) The interfacial shear storage modulus ($G_i$') and loss modulus ($G_i$'') as a function of strain for Rubisco proteins (RU ● and RA ■). (B) Normalized Lissajous plots (black curves) and their decomposed elastic torque curves (red lines) at strains of 0.5, 5, 16, 30, and 100% and a fixed frequency of 0.1 Hz for rubisco proteins (RU and RA). (C) The dissipation ratio of the Lissajous plots for Rubisco as a function of strain. All samples were prepared at a soluble protein concentration of 0.1 wt% in 20 mM pH 7.0 phosphate buffer.

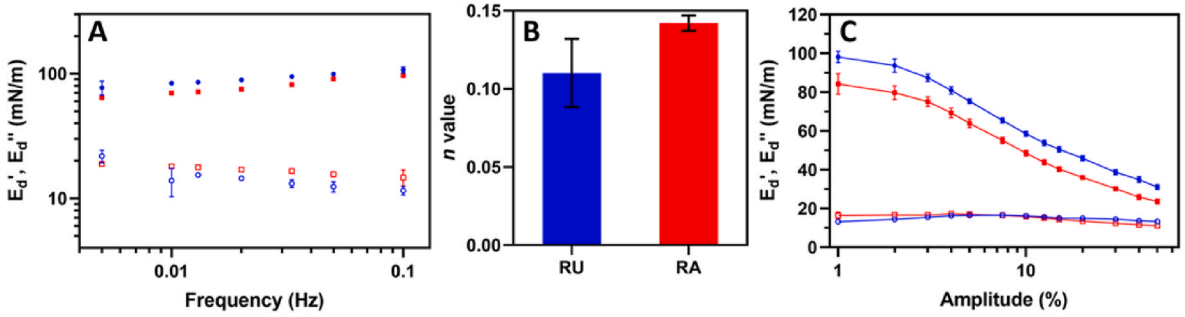


**Fig. 6.** Interfacial dilatational storage modulus ($E_d$') and loss modulus ($E_d$'') for Rubisco (RU ● and RA ■) as a function of frequency (A), and amplitude (C). (B) The values of the power-law exponent n obtained from the interfacial dilatational frequency sweep at a fixed strain of 3% for Rubisco (RU and RA). All solutions were prepared at 0.1 wt% in 20 mM pH 7.0 phosphate buffer.

RU-stabilized interface has higher residual elasticity than the RA-stabilized interface. It is worth noting that the $E_d$' of the RU-stabilized air-water interface (38.7 mN/m) at a deformation amplitude of 30% is distinctly higher than the $E_d$' (~30 mN/m) of interfaces stabilized by many other proteins, such as lupin protein (Ma, Shen, Habibi, & Sagis, 2024), napin (Shen, Yang, et al., 2023), and rapeseed protein (Yang et al., 2021), suggesting that the interface stabilized by native Rubisco protein is also more resistive to large dilatational deformations than the interfaces stabilized by those proteins.

To gain a deeper understanding of the non-linear behavior of RU and RA at the air-water interface at large deformations, we constructed Lissajous plots at deformation amplitudes from 5% to 50%. At 5% deformation amplitude, the Lissajous plots of RU and RA are narrow and nearly elliptical, indicating linear viscoelastic behavior and the dominance of elastic behavior. With increasing amplitudes, the Lissajous plots of RU and RA become wider and asymmetric, suggesting an increased viscous contribution and the occurrence of non-linear behavior. At 50% deformation, we first observed a steep increase of surface pressure at the start of expansion (the left corner of a Lissajous plot), suggesting a high initial interfacial stiffness. This is followed by a substantially reduced slope of the Lissajous plots upon further expansion, known as strain softening. Upon compression, strain hardening was observed, due to the increased surface density and the jamming of proteins at the air-water interface. The Lissajous plots of RU at 30–50% deformation amplitudes show stronger strain hardening than the ones of RA, suggesting a higher resistance against compression. This higher stiffness of the interface is also indicated by the macroscopic residual structure after the rising bubble stabilized by RU was expelled (Fig. S1). Overall, the Lissajous plots of both RU and RA exhibit distinctly different non-linear behavior, and we further decomposed these Lissajous plots using the general stress decomposition method (de Groot, Yang, & Sagis, 2023) to elucidate their non-linear rheological behavior.

### 3.3.3. *General stress decomposition*

The asymmetries in Lissajous plots at large deformations in Fig. 7, are unique for dilatational rheology, since in shear rheology Lissajous plots at large strains are always symmetric with respect to the origin (Fig. 5C). This difference in interfacial shear and dilatational rheology is caused by the fact that in dilatation surface density changes during deformation, and hence the response in compression (where density increases) differs from the response in expansion (where density decreases). When Fourier transforming a nonlinear stress signal, the spectrum in shear rheology shows only odd harmonics, while the spectrum from dilatational rheology, because of the asymmetry between compression and expansion, displays both odd and even harmonics. In the general stress decomposition (GSD) we separate the odd and even harmonics, and split the contribution to the stress from the odd harmonics in an elastic and viscous contribution ($\tau_1$ and $\tau_2$, respectively), and similarly split the contribution from the even harmonics into $\tau_3$ and $\tau_4$ (i.e., a viscous and elastic contribution, respectively) (de Groot, Sagis, & Yang, 2023). The asymmetries in the dilatational Lissajous plots in dilatational rheology originate from the even harmonics that represent the contributions to the surface stress caused by surface density changes, and the higher odd harmonics describe the contributions induced by interfacial network changes (de Groot, Yang, & Sagis, 2023).

At a deformation amplitude of 40%, the odd harmonics ($\tau_1 + \tau_2$) of RU and RA comprise a closed rhomboidal loop with a pronouncedly distorted elastic component ($\tau_1$), where intracycle strain hardening can be observed towards maximum expansion, due to the stretching of the residual interfacial structure (Fig. 8B–C and F-G). RU clearly shows more

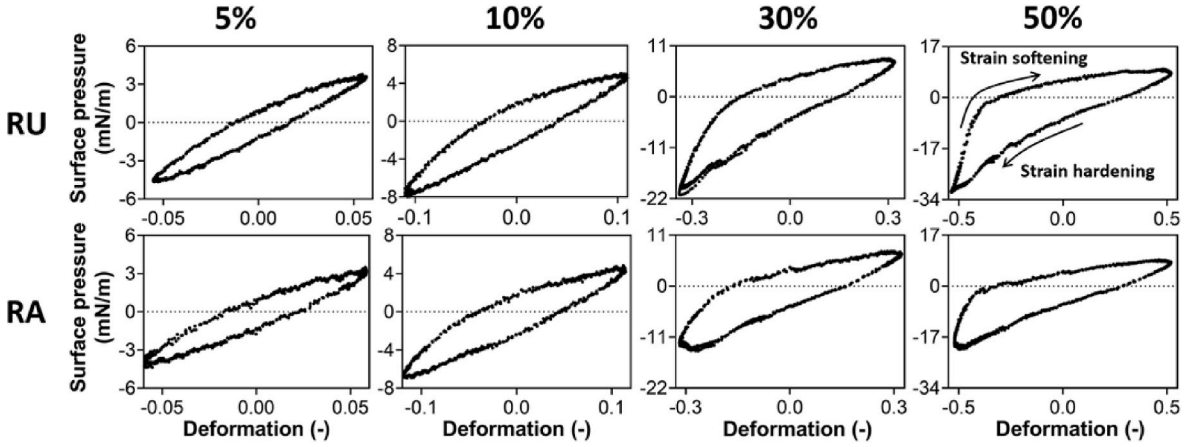


**Fig. 7.** Lissajous plots of surface pressure as a function of applied deformation (5–50%) for Rubisco (RU and RA). All samples were measured in triplicate, and one representative plot is shown.

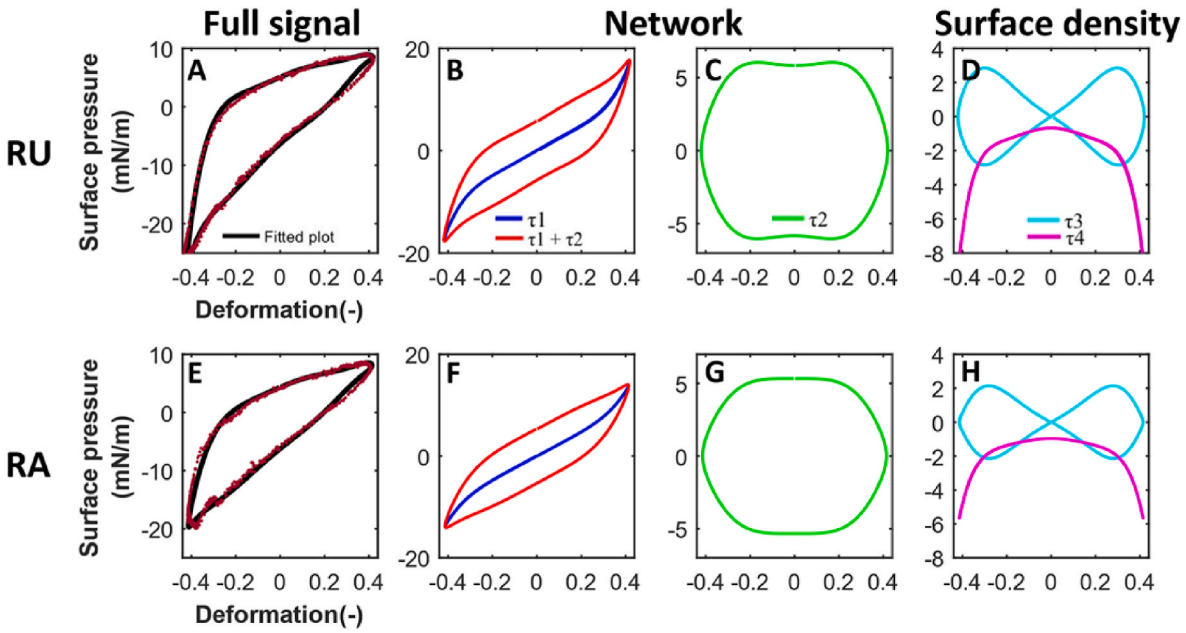


**Fig. 8.** Decomposed Lissajous plots of Rubisco (RU and RA) at a strain of 40%. The fitted full signal is shown in black (——), $\tau_1$ is shown in dark blue (——), $\tau_1 + \tau_2$ is shown in red (——), $\tau_2$ is shown in green (——), $\tau_3$ is shown in cyan (——), and $\tau_4$ is shown in magenta (——).

plastic behavior (Fig. 8C) and a more distorted $\tau_1$ curve (Fig. 8B) than RA, suggesting that RU has stronger in-plane interactions, and its interfacial structure was more extensively disrupted at 40% deformation. These phenomena agree with the wider $\tau_2$ loop of RU than that of RA, which indicates higher energy dissipation at the RU-stabilized interface due to interfacial structure disruption. The contributions from even harmonics ($\tau_3$ & $\tau_4$) in the interfacial dilatational rheological behavior of RU and RA are shown in Fig. 8D and H. The decomposed stress of $\tau_3$ is a lemniscate loop, and $\tau_4$ is a single downward curve. The main difference between RU (Fig. 8D) and RA (Fig. 8H) is in the plot of $\tau_4$, which is more negative for RU-stabilized interfaces towards maximum intra-cycle strain, which indicates the response of the RU-stabilized interface is more resistive to interfacial density changes. RU has a similar $\tau_3$ curve with RA, suggesting similar adsorption/desorption behavior during the large dilatational deformation.

We further quantified the contributions from odd harmonics and even harmonics to the overall dilatational stress response of the interfaces formed by RU and RA with the GSD method. Regarding odd harmonics, the secant modulus ($E_{\tau 1L}$) (Fig. 9A), which is the slope of the line connecting the origin with the maximum value of $\tau_1$, was used to indicate the stiffness of the interface. All interfaces show a decreasing trend of $E_{\tau 1L}$ with increased amplitudes, indicating the disruption of the interfacial structure. The $E_{\tau 1L}$ of RU was significantly higher than RA at all amplitudes, suggesting that RU formed a stiffer air-water interface than RA. We also calculated the energy dissipation from network disruption (Fig. 9D), which is the total area enclosed by the $\tau_2$ loop (denoted as $U_{\tau 2}$) (Fig. 8C and G). RU clearly shows a higher value of $U_{\tau 2}$ than RA, indicating stronger in-plane protein-protein interactions that

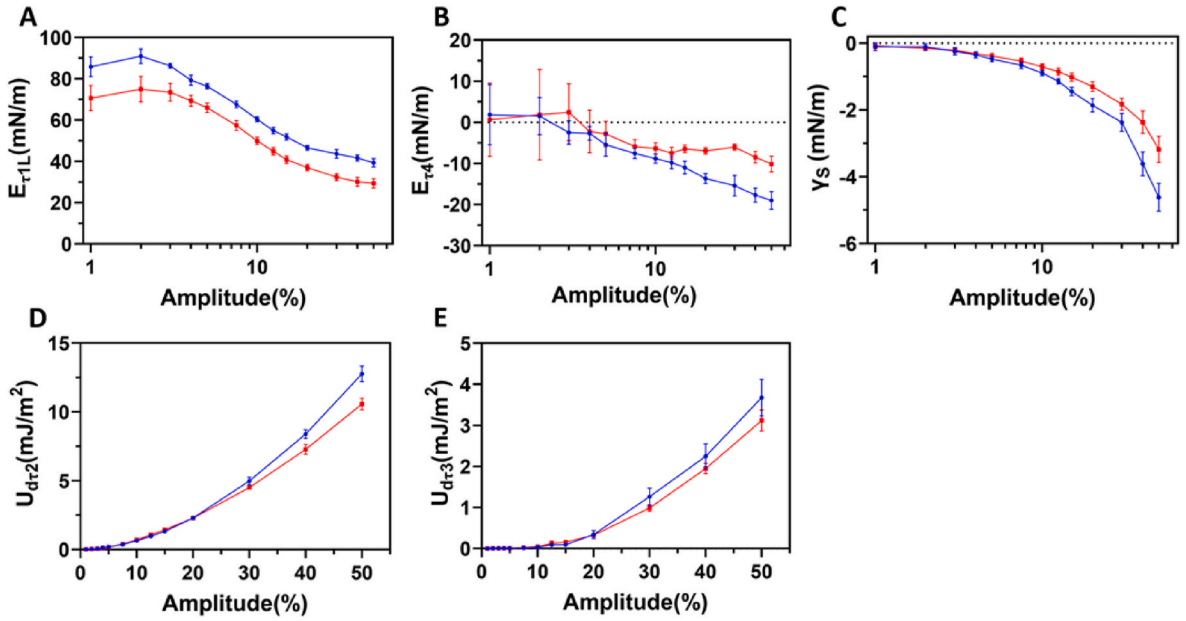


**Fig. 9.** $E_{\tau 1L}$ (A), $E_{\tau 4}$ (B), $\gamma_s$ (C), $U_{d\tau 2}$ (D), and $U_{d\tau 3}$ (E) as a function of amplitude (%) for the air-water interface stabilized with Rubisco (RU ● and RA ■).

require more energy to disrupt the interfacial structure.

As for the even harmonics, the secant modulus $E_{\tau 4}$ of the $\tau_4$ curve quantifies the contribution to the interfacial stress resulting from density changes. As shown in Fig. 9B, RU had a more negative $E_{\tau 4}$ modulus at the amplitudes from 10% to 50% than RA, indicating higher resistance against interfacial density changes for the RU-stabilized interface. The vertical shift of the $\tau_4$ curve from the origin is characterized by the parameter $\gamma_s$, and its magnitude measures the extent that the system is driven out of the equilibrium by the oscillations. The $\gamma_s$ values of RU and RA increase with increased amplitudes, and RU always has a larger value of $\gamma_s$, suggesting that the RU-stabilized interface tends to be driven further away from its equilibrium state. Compared with RA, the higher $E_{\tau 4}$ and $\gamma_s$ values of RU probably indicate that the RU-stabilized interface is denser and has lower in-plane protein mobility, causing slower in-plane relaxation. As a result, the RU-stabilized interface cannot quickly restore itself to the equilibrium state during oscillations. We also calculated the energy dissipation resulting from surface density changes (denoted as $U_{\tau 3}$) (Fig. 9E). RU shows a slightly wider $\tau_3$ loop and a higher value of $U_{\tau 3}$ than RA, which indicates RU has a somewhat higher extent of exchange between bulk and interfaces which is probably related to the smaller size of RU (Fig. 3A).

Overall, RU-stabilized air-water interfaces had more pronounced contributions from both odd and even harmonics than the ones stabilized with RA. The resulting RU-stabilized interfaces were stiffer and probably denser than RA-stabilized interfaces.

### 3.4. Air-water interfacial microstructure of rubisco proteins

We prepared Langmuir-Blodgett films at surface pressures of 10 mN/m and 25 mN/m to investigate the air-water interfacial structure of RU and RA, and these films were observed under AFM. The AFM images were then quantitatively characterized by performing protein network analysis using AngioTool 64 software (Bernklau et al., 2016) and calculating the pair correlation function for protein domain size and structure heterogeneity analysis in image J (Munialo, van der Linden, Ako, & de Jongh, 2015). Parameters such as vessel area, junction density, average vessel length, branching rate, end-point rate, and lacunarity were determined by the AngioTool 64 software. The vessel area indicates the overall area occupied by the protein network. The junction density is calculated from the total number of junction points in the protein network divided by the vessel area and is related to the connectivity of the protein network. The lacunarity indicates the relative variance of voids in the protein network, which is related to structural heterogeneity. A higher lacunarity indicates a more heterogeneous structure, and vice versa.

In the AFM micrographs, the protein-rich regions were indicated by bright regions, and all films clearly show heterogeneous structures (Fig. 10). In the view of 2 × 2 $\mu m^2$, the films formed at a higher surface pressure (25 mN/m) were denser than those at a lower surface pressure (10 mN/m). At the surface pressure of 25 mN/m, RU appears to form a less heterogeneous interfacial structure than RA, where small protein clusters dominate the interfacial structure.

We further performed protein network analysis using AngioTool 64 software as shown in Fig. 11. At the surface pressure of 25 mN/m, compared to RA, RU formed denser network structures with higher connectivity between protein clusters and longer protein threads as indicated by its higher vessel percentage area (Fig. 11A), higher junction density (Fig. 11B) and lower end point rates (Fig. 11E), and longer average vessel length (Fig. 11C). Again, the lower degree of heterogeneity in the RU-stabilized interface was confirmed by its slightly lower mean lacunarity (Fig. 11F). These results indicate that RU forms a denser air-water interface with a more fine-stranded structure than RA. We further imaged the films (25 mN/m) at a larger magnification of 0.35 × 0.35 $\mu m^2$ (Fig. 10 D&H). Locally, RA seems to form larger protein aggregates with a size of around 34 nm (Fig. S2B), while RU forms finer protein strands with a size of around 11 nm (Fig. S2A). The pair correlation function was subsequently used to determine the protein domain size in these films at a surface pressure of 25 mN/m. Overall, RU tends to have a smaller protein domain size of 52.1 ± 6.4 nm than RA (67.6 ± 19.8 nm). The differences in protein domain sizes of RU and RA might be related to their protein conformations. RU had a more flexible protein structure than RA, which can undergo more structure rearrangement at the interface and thus form finer protein-stranded network structures.

We found close relationships between the interfacial structural and rheological properties of RU and RA. RA tends to form a coarser air-water interface with larger protein aggregates with lower network connectivity, which explains their lower interfacial stiffness in response to both shear and dilatational deformation than RU. In contrast, RU

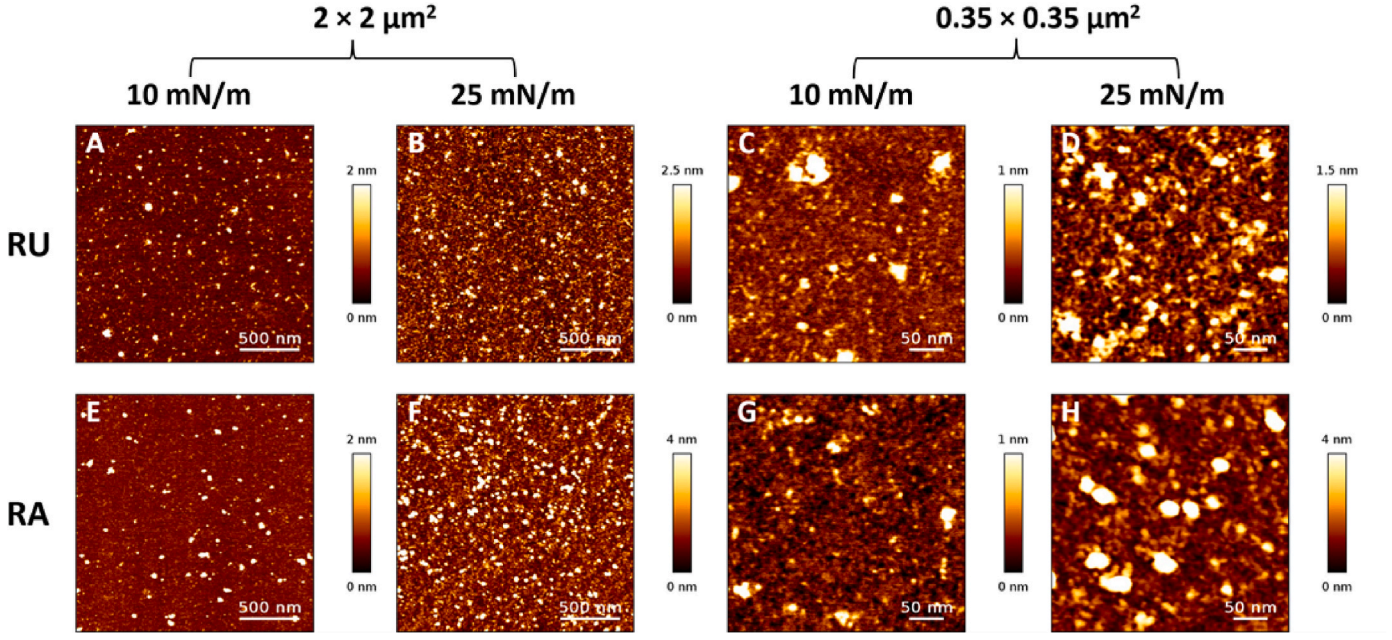


**Fig. 10.** AFM images of Langmuir-Blodgett films for Rubisco (RU and RA) prepared at a surface pressure of 10 mN and 25 mN over 2 × 2 $\mu m^2$ areas (A-B and E-F) and 0.35 × 0.35 $\mu m^2$ areas (C-D and G-H) in a lateral resolution of 512 × 512 $pixels^2$.

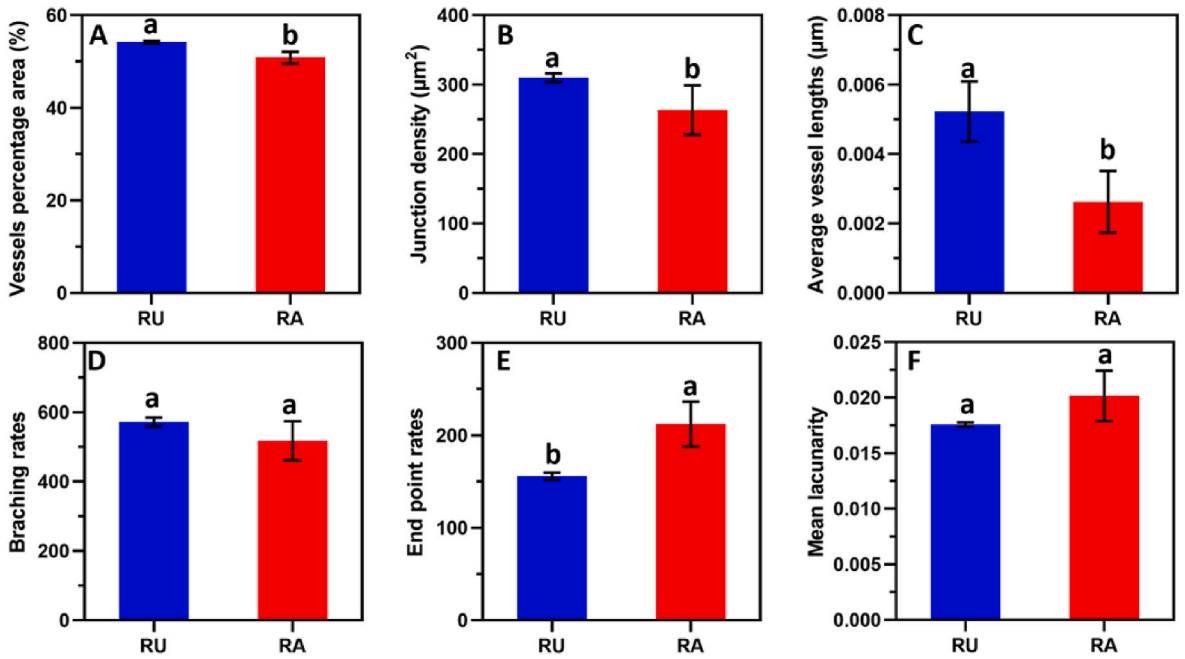


**Fig. 11.** Protein network analysis determined by AngioTool for Rubisco (RU and RA) at a surface pressure of 25 mN/m (A) vessel percentage area (%); (B) junction density ($\mu m^2$); (C) average vessel length (μm); (D) branching rates; (E) end point rates; (F) mean lacunarity. One-way ANOVA with Duncan test was used to test the significant levels among samples, and different letters (a–b) represent significant differences ($p < 0.05$).

forms a more compact and fine-stranded interface with higher connectivity, which in turn explains its higher interfacial stiffness in shear and dilatation. The RU-stabilized interface has a stronger contribution from odd harmonics in dilatations with higher $E_{\tau 1L}$ than RA, which may indicate the formation of a more gel-like interface. The denser air-water interface of RU at a surface pressure of 25 mN/m from AFM images was again in line with the results from the GSD, where the RU-stabilized air-water interface has more contributions from even harmonics than RA.

Those differences in air-water interfacial behavior between RU and RA could be further correlated to the protein's molecular properties: (1) RU had a smaller particle size than RA (Fig. 2A). Smaller particles have a higher area-to-volume ratio compared to larger particles. This means that there might be more active sites available in RU for interaction with the surrounding proteins at the air-water interface. As a result, RU has stronger in-plane interactions and formed a denser and more tightly packed air-water interface than RA; (2) RU was less negatively charged than RA (Fig. 2B). The air-water interfaces were previously proved to be strongly negatively charged, due to the accumulation of $OH^-$ near the interface (Beattie, Djerdjev, & Warr, 2009; Li & Somasundaran, 1991; Manciu & Ruckenstein, 2012). The slightly lower negative charges of RU result in a lower electrostatic repulsion between proteins at the air-water interface and thus facilitate the formation of a denser and stiffer interface; (3) RU is conformationally more flexible due to the lack of disulfide bonds between protein subunits, which facilitates the structural rearrangement of proteins and promotes protein-protein interactions at the interface. While RA has more rigid protein structures due to the abundance of intra/intermolecular disulfide bonds (Fig. 1), which limits its structural rearrangement and interactions with counterparts at the interface. Previous studies also showed that soy protein with higher conformational flexibility could more rapidly adsorb to interfaces and form stiffer interfaces (Cao et al., 2022; L.-J. Luo, Liu, & Tang, 2013).

### 3.5. Foaming properties of rubisco

The foaming properties including foamability and foam stability of Rubisco proteins (RU and RA) were evaluated by foam overrun and foam half-life time, respectively. RU and RA showed a comparable foam overrun of ~400% (Fig. 12A), indicating a high foamability of these two Rubisco proteins. The protein foamability is mainly determined by two factors: (1) the adsorption rate of proteins to the air-water interface and (2) the interfacial stability of the air bubble against shear and dilatational deformation during preparation (whipping in this study). Although RA showed a slower adsorption rate to the air-water interface than RU (Fig. 3A) due to its larger particle size, more negative zeta potential value and rigid molecular structure, RA could form a stiffer air-water interface in response to both shear and dilatational deformation on the short time scales of adsorption (Fig.s 4A and 6A), which is because its higher surface hydrophobicity promotes protein-protein in-plane interactions. These two factors are expected to both play a role and apparently offset each other, resulting in a comparable foamability of RU and RA.

Rubisco extracts in this study show much higher foamability than in early studies, where Rubisco was extracted from other leaves, such as from broccoli leaf (~170%) (Rawiwan et al., 2024), cabbage leaf (~170%) (Rawiwan et al., 2024), radish leaf (~160%) (Rawiwan et al., 2024), and sugar beet leaf (10–40%) (Martin et al., 2019). The high foamability of Rubisco in our study might be due to its high purity (78.6–90.7%) and solubility (91.7–95.8%). Additionally, Rubisco extracts in this study also show higher foamability (~400%) than many other plant proteins, including lentil protein (285%) (Shen, Peng, et al., 2023), rapeseed proteins (cruciferin ~320%) (Shen, Yang, et al., 2023), pea proteins (globulin 61% and albumin 258%) (Kornet, Yang, Venema, van der Linden, & Sagis, 2022), and mung bean protein (42% at 0.1% protein and 200% at 1% protein) (Yang et al., 2023). The excellent foamability of Rubisco shows its potential as a novel foaming agent in the food industry.

RU-stabilized foam displays a considerably longer half-life time (152 min) than RA-stabilized foams (94 min) (Fig. 12B). The foam half-life is mostly affected by the air-water interfacial stiffness of the air bubbles. As shown in Fig.s 5 and 6, the RU-stabilized air-water interface was stiffer in response to both shear and dilatational deformations than that stabilized by RA, which could explain the longer foam half-life time of RU. Additionally, the higher interfacial thickness (Fig. S3) and denser air-water interface with more network connectivity of RU is also

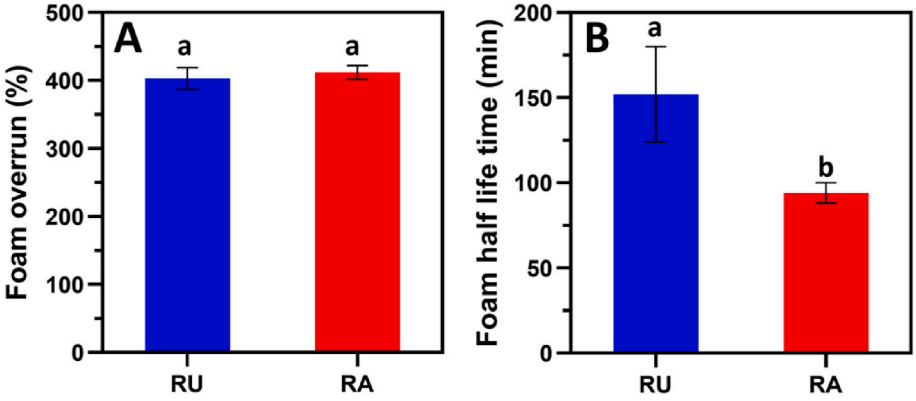


**Fig. 12.** Foam overrun (%) and foam half-life time (min) of Rubisco (RU and RA). The protein dispersions were prepared at 0.1 wt% in 20 mM pH 7.0 phosphate buffer. One-way ANOVA with Duncan test was used to test the significant levels among samples, and different letters (a–b) represent significant differences ($p < 0.05$).

conducive to its higher foam stability than RA. Both RU- and RA-stabilized foams mostly finished the liquid drainage within 20 min, thus liquid drainage should not be the main factor affecting the foam stability in this study.

Rubisco extracts in this study also show higher foam stability than those extracted from other leaves, such as from broccoli, cabbage, and radish leaves (~60 min) (Rawiwan et al., 2024) and from sugar beet leaf (~15 min) (Martin et al., 2019). Besides, the mildly extracted Rubisco (RU) also displays higher foam stability than the mildly extracted lentil proteins (115 min) (Shen, Peng, et al., 2023), rapeseed proteins (20–60 min) (Yang et al., 2021), pea protein concentrate (14 min) (Kornet et al., 2022), and mung bean protein (globulins ~40 min) (Yang et al., 2023). The resulting excellent foaming properties of RU benefit from its fast adsorption to the interface as well as the formation of stiff, dense, and thick air-water interfaces as found from previous interfacial adsorption, rheology, and structure measurements.

Overall, the extensive extraction method caused protein denaturation and aggregation, thus leading to a less stiff air-water interface and less stable foam. In comparison, the mildly extracted method better-retained protein nativity and increased protein conformational flexibility, which resulted in a stiffer air-water interface and more stable foam. Although the extensively extracted Rubisco behaved less well in interfacial and foam stabilization than the mildly extracted Rubisco, it still formed a stiff air-water interface with high initial elastic modulus and excellent foamability. In this case, denaturation or aggregation of proteins may not necessarily link to the poor foaming properties, such as foamability; instead, the denatured and aggregated proteins can still interact with each other at the interface through the interactions between exposed hydrophobic patches and form a stiff interface. Nevertheless, the native and flexible Rubisco molecular structure is more favorable for forming a stiff interface and beneficial to foam stabilization, compared to the denatured and aggregated counterpart.

## 4. Conclusions

In this study, we systematically investigated the influence of the molecular conformation of Rubisco proteins altered by two distinct extraction methods, the ultrafiltration method (mild) and acid precipitation-alkaline redispersion method (extensive), on their air-water interface and foam stabilization behavior. The mildly extracted Rubisco (RU) adsorbed faster to the air-water interface than the extensively extracted Rubisco (RA), however, RA could develop stiffer air-water interfaces in the early adsorption phase to both shear and dilatational deformations. These two factors offset and led to a comparable foam overrun (~400%) between RU and RA. After 3 h of adsorption, RU formed finer protein-stranded network at the interfaces that were stiffer and more gel-like, which gave it higher foam stability. Conversely, RA formed more heterogeneous air-water interfaces with larger protein aggregates, which caused less stiff interfaces and less stable foam. These differences in interfacial structure were clearly related to the different molecular structures of RU and RA. RU has a more flexible protein structure due to the lack of S-S bonds, while RA has a more rigid protein structure due to the abundance of S-S bonds. The more flexible structures of RU caused easier protein structure rearrangement at the interface, leading to stiffer, denser, and finer interfacial structures. Our work provides new insights into the air-water interface and foam stabilization mechanisms of Rubisco regarding its molecular conformation, and how this is changed by extensive and mild extraction methods. This study provides key findings for obtaining good foaming performance by tuning the molecular structures of proteins. It might also guide the development of improved extraction/treatment methods to obtain ideal molecular structures of proteins for foam stabilization.

In addition to being a good foamer, Rubisco was also identified as an excellent emulsifier (Delahaije, Kiskini, & Wierenga, 2022; Lamsal et al., 2007; Pérez-Vila, Fenelon, O'Mahony, & Gómez-Mascaraque, 2024; Tan, Lee, Martens, & McClements, 2022). Due to the large difference in the nature of the air-water interface and oil-water interface, the effects of molecular properties of Rubisco on behavior at the oil-water interface and on emulsion stabilization might be significantly different from those at the air-water interface and in foam. This will be further investigated in part II of this study.

## CRediT authorship contribution statement

**Xingfa Ma:** Writing – review & editing, Writing – original draft, Visualization, Validation, Methodology, Investigation, Formal analysis, Data curation, Conceptualization. **Thomas van Polen:** Methodology, Investigation. **Mehdi Habibi:** Writing – review & editing, Supervision. **Jasper Landman:** Writing – review & editing, Supervision. **Leonard M. C. Sagis:** Writing – review & editing, Supervision. **Penghui Shen:** Writing – review & editing, Writing – original draft, Validation, Project administration, Methodology, Investigation, Formal analysis, Conceptualization.

## Declaration of competing interest

The authors declare that they have no known competing financial interests or personal relationships that could have appeared to influence the work reported in this paper.

## Acknowledgments

X. Ma acknowledges the funding from China Scholarship Council (CSC NO. 202207940007). P. Shen acknowledges the funding from

China Scholarship Council (CSC NO. 202006150032).

## Appendix A. Supplementary data

Supplementary data to this article can be found online at https://doi.org/10.1016/j.foodhyd.2024.110783.

## Data availability

Data will be made available on request.

## References


Andersson, I., & Backlund, A. (2008). Structure and function of rubisco. *Plant Physiology and Biochemistry, 46*(3), 275–291.

Barbeau, W. E., & Kinsella, J. E. (1988). Ribulose bisphosphate carboxylase/oxygenase (rubisco) from green leaves-potential as a food protein. *Food Reviews International, 4*(1), 93–127.

Barta, C., Carmo-Silva, A. E., & Salvucci, M. E. (2011). Purification of Rubisco activase from leaves or after expression in Escherichia coli. *Photosynthesis Research Protocols*, 363–374.

Beattie, J. K., Djerdjev, A. M., & Warr, G. G. (2009). The surface of neat water is basic. *Faraday Discussions, 141*, 31–39.

Bernklau, I., Lucas, L., Jekle, M., & Becker, T. (2016). Protein network analysis—a new approach for quantifying wheat dough microstructure. *Food Research International, 89*, 812–819.

Binder, B. J., & Simpson, M. J. (2013). Quantifying spatial structure in experimental observations and agent-based simulations using pair-correlation functions. *Physical Review E, 88*(2), Article 022705.

Buchmann, L., Bertsch, P., Böcker, L., Krähenmann, U., Fischer, P., & Mathys, A. (2019). Adsorption kinetics and foaming properties of soluble microalgae fractions at the air/water interface. *Food Hydrocolloids, 97*, Article 105182.

Buyel, J., Twyman, R., & Fischer, R. (2015). Extraction and downstream processing of plant-derived recombinant proteins. *Biotechnology Advances, 33*(6), 902–913.

Cao, W., Gao, R., Wan, X., He, Z., Chen, J., Wang, Y., et al. (2022). Effects of globular and flexible structures on the emulsifying and interfacial properties of mixed soy proteins. *Food Hydrocolloids, 127*, Article 107539.

de Groot, A., Sagis, L. M., & Yang, J. (2023). White asparagus stem proteins, from waste to interface stabilizer in food foams. *Food Hydrocolloids, 109218*.

de Groot, A., Yang, J., & Sagis, L. M. (2023). Surface stress decomposition in large amplitude oscillatory interfacial dilatation of complex interfaces. *Journal of Colloid and Interface Science, 638*, 569–581.

Delahaije, R. J. B. M., Kiskini, A., & Wierenga, P. A. (2022). Towards predicting the emulsion properties of plant protein extracts from sugar beet (Beta vulgaris L.) leaf and soybean (Glycine max). *Colloids and Surfaces A: Physicochemical and Engineering Aspects, 646*, Article 128950.

Douillard, R., & De Mathan, O. (1994). Leaf protein for food use: Potential of rubisco. In *New and developing sources of food proteins* (pp. 307–342). Springer.

Ellis, R. J. (1979). The most abundant protein in the world. *Trends in Biochemical Sciences, 4*(11), 241–244.

Ewoldt, R. H., Hosoi, A., & McKinley, G. H. (2008). New measures for characterizing nonlinear viscoelasticity in large amplitude oscillatory shear. *Journal of Rheology, 52*(6), 1427–1458.

Ge, J., Sun, C.-X., Mata, A., Corke, H., Gan, R.-Y., & Fang, Y. (2021). Physicochemical and pH-dependent functional properties of proteins isolated from eight traditional Chinese beans. *Food Hydrocolloids, 112*, Article 106288.

Grácio, M., Oliveira, S., Lima, A., & Ferreira, R. B. (2023). RuBisCO as a protein source for potential food applications: A review. *Food Chemistry, 419*, Article 135993.

Heppner, S., & Livney, Y. D. (2023). Green leaves as a promising source for sustainable food protein: Seeking the productivity-functionality balance. *Trends in Food Science & Technology*, Article 104207.

Hinderink, E. B., Meinders, M. B., Miller, R., Sagis, L., Schroën, K., & Berton-Carabin, C. C. (2022). Interfacial protein-protein displacement at fluid interfaces. *Advances in Colloid and Interface Science, 305*, Article 102691.

Jeurink, P. V., & Savelkoul, H. F. (2006). Induction and regulation of allergen-specific IgE. In *Allergy matters* (pp. 13–27). Springer.

Jiang, J., Xiong, Y. L., & Chen, J. (2010). pH shifting alters solubility characteristics and thermal stability of soy protein isolate and its globulin fractions in different pH, salt concentration, and temperature conditions. *Journal of Agricultural and Food Chemistry, 58*(13), 8035–8042.

Kobbi, S., Bougatef, A., Le Flem, G., Balti, R., Mickael, C., Fertin, B., et al. (2017). Purification and recovery of RuBisCO protein from alfalfa green juice: Antioxidative properties of generated protein hydrolysate. *Waste and biomass valorization, 8*, 493–504.

Kornet, R., Yang, J., Venema, P., van der Linden, E., & Sagis, L. M. (2022). Optimizing pea protein fractionation to yield protein fractions with a high foaming and emulsifying capacity. *Food Hydrocolloids, 126*, Article 107456.

Kristinsson, H. G., & Hultin, H. O. (2003). Changes in conformation and subunit assembly of cod myosin at low and high pH and after subsequent refolding. *Journal of Agricultural and Food Chemistry, 51*(24), 7187–7196.

Lamsal, B., Koegel, R., & Gunasekaran, S. (2007). Some physicochemical and functional properties of alfalfa soluble leaf proteins. *Lwt-Food Science and Technology, 40*(9), 1520–1526.

Li, C., & Somasundaran, P. (1991). Reversal of bubble charge in multivalent inorganic salt solutions—effect of magnesium. *Journal of Colloid and Interface Science, 146*(1), 215–218.

Lucassen, J., & Van Den Tempel, M. (1972). Dynamic measurements of dilational properties of a liquid interface. *Chemical Engineering Science, 27*(6), 1283–1291.

Luo, L.-J., Liu, F., & Tang, C.-H. (2013). The role of glycinin in the formation of gel-like soy protein-stabilized emulsions. *Food Hydrocolloids, 32*(1), 97–105.

Ma, X., Shen, P., Habibi, M., & Sagis, L. M. (2024). Interfacial properties and functionality of lupin protein-pectin complexes at the air-water interface. *Food Hydrocolloids, 110050*.

Manciu, M., & Ruckenstein, E. (2012). Ions near the air/water interface: I. Compatibility of zeta potential and surface tension experiments. *Colloids and Surfaces A: Physicochemical and Engineering Aspects, 400*, 27–35.

Martin, A. H., Castellani, O., de Jong, G. A., Bovetto, L., & Schmitt, C. (2019). Comparison of the functional properties of RuBisCO protein isolate extracted from sugar beet leaves with commercial whey protein and soy protein isolates. *Journal of the Science of Food and Agriculture, 99*(4), 1568–1576.

Martin, A. H., Grolle, K., Bos, M. A., Stuart, M. A. C., & van Vliet, T. (2002). Network forming properties of various proteins adsorbed at the air/water interface in relation to foam stability. *Journal of Colloid and Interface Science, 254*(1), 175–183.

Martin, A. H., Nieuwland, M., & de Jong, G. A. (2014). Characterization of heat-set gels from RuBisCO in comparison to those from other proteins. *Journal of Agricultural and Food Chemistry, 62*(44), 10783–10791.

Moreno, J., García-Murria, M. J., & Marín-Navarro, J. (2008). Redox modulation of Rubisco conformation and activity through its cysteine residues. *Journal of Experimental Botany, 59*(7), 1605–1614.

Muller, T., Bernier, M.-È., & Bazinet, L. (2023). Optimization of water lentil (duckweed) leaf protein purification: Identification, structure, and foaming properties. *Foods, 12*(18), 3424.

Munialo, C. D., van der Linden, E., Ako, K., & de Jongh, H. H. (2015). Quantitative analysis of the network structure that underlines the transitioning in mechanical responses of pea protein gels. *Food Hydrocolloids, 49*, 104–117.

Negi, A. S., & Osuji, C. O. (2010). Time-resolved viscoelastic properties during structural arrest and aging of a colloidal glass. *Physical Review E, 82*(3), Article 031404.

Nynäs, A.-L., Newson, W. R., Langton, M., Wouters, A. G., & Johansson, E. (2023). Applicability of leaf protein concentrates from various sources in food: Solubility at food-relevant pH values and air-water interfacial properties. *Lebensmittel-Wissenschaft und -Technologie, 184*, Article 114962.

Parsegian, V. A., & Rand, R. P. (2019). Forces governing lipid interaction and rearrangement. In *Membrane fusion* (pp. 65–85). CRC Press.

Pearce, F. G., & Brunke, J. E. (2023). Is now the time for a rubiscuit or ruburger? Increased interest in rubisco as a food protein. *Journal of Experimental Botany, 74*(2), 627–637.

Pérez-Vila, S., Fenelon, M. A., O'Mahony, J. A., & Gómez-Mascaraque, L. G. (2024). The emulsifying properties of protein extracts from perennial ryegrass (Lolium perenne L.) depend on the extraction method. *Food Hydrocolloids, 152*, Article 109917.

Poole, L. B. (2015). The basics of thiols and cysteines in redox biology and chemistry. *Free Radical Biology and Medicine, 80*, 148–157.

Rawiwan, P., & Quek, S. Y. (2024). Physicochemical and functional attributes of RuBisCo-enriched Brassicaceae leaf protein concentrates. *Food Hydrocolloids*, Article 109887.

Sagis, L. M., & Fischer, P. (2014). Nonlinear rheology of complex fluid–fluid interfaces. *Current Opinion in Colloid & Interface Science, 19*(6), 520–529.

Sagis, L. M., Liu, B., Li, Y., Essers, J., Yang, J., Moghimikheirabadi, A., et al. (2019). Dynamic heterogeneity in complex interfaces of soft interface-dominated materials. *Scientific Reports, 9*(1), 2938.

Seckler, R., & Jaenicke, R. (1992). Protein folding and protein refolding. *The FASEB Journal, 6*(8), 2545–2552.

Sheen, S. J., & Sheen, V. L. (1985). Functional properties of fraction 1 protein from tobacco leaf. *Journal of Agricultural and Food Chemistry, 33*(1), 79–83.

Shen, P., Peng, J., Sagis, L. M., & Landman, J. (2023). Air-water interface properties and foam stabilization by mildly extracted lentil protein. *Food Hydrocolloids*, Article 109342.

Shen, P., Yang, J., Nikiforidis, C. V., Mocking-Bode, H. C., & Sagis, L. M. (2023). Cruciferin versus napin–Air-water interface and foam stabilizing properties of rapeseed storage proteins. *Food Hydrocolloids, 136*, Article 108300.

Tan, R. Y. H., Lee, C. S., Pichika, M. R., Cheng, S. F., & Lam, K. Y. (2022). PH responsive polyurethane for the advancement of biomedical and drug delivery. *Polymers, 14*(9), 1672.

Tan, Y., Lee, P. W., Martens, T. D., & McClements, D. J. (2022). Comparison of emulsifying properties of plant and animal proteins in oil-in-water emulsions: Whey, soy, and RuBisCo proteins. *Food Biophysics, 17*(3), 409–421.

Tang, C.-H. (2017). Emulsifying properties of soy proteins: A critical review with emphasis on the role of conformational flexibility. *Critical Reviews in Food Science and Nutrition, 57*(12), 2636–2679.

Venkataraman, S., Rajendran, D. S., Kumar, P. S., Vo, D.-V. N., & Vaidyanathan, V. K. (2022). Extraction, purification and applications of biosurfactants based on microbial-derived glycolipids and lipopeptides: A review. *Environmental Chemistry Letters*, 1–22.

Verruto, V. J., Le, R. K., & Kilpatrick, P. K. (2009). Adsorption and molecular rearrangement of amphoteric species at oil– water interfaces. *The Journal of Physical Chemistry B, 113*(42), 13788–13799.

Wierenga, P., & Gruppen, H. (2010). New views on foams from protein solutions. *Current Opinion in Colloid & Interface Science, 15*(5), 365–373.
Wierenga, P. A., Meinders, M. B., Egmond, M. R., Voragen, F. A., & de Jongh, H. H. (2003). Protein exposed hydrophobicity reduces the kinetic barrier for adsorption of ovalbumin to the air− water interface. *Langmuir, 19*(21), 8964–8970.
Yang, J., Faber, I., Berton-Carabin, C. C., Nikiforidis, C. V., van der Linden, E., & Sagis, L. M. (2021). Foams and air-water interfaces stabilised by mildly purified rapeseed proteins after defatting. *Food Hydrocolloids, 112*, Article 106270.
Yang, J., Yang, Q., Waterink, B., Venema, P., de Vries, R., & Sagis, L. M. (2023). Physical, interfacial and foaming properties of different mung bean protein fractions. *Food Hydrocolloids, 143*, Article 108885.
Zhang, W., Grimi, N., Jaffrin, M. Y., Ding, L., & Tang, B. (2017). A short review on the research progress in alfalfa leaf protein separation technology. *Journal of Chemical Technology & Biotechnology, 92*(12), 2894–2900.
Zhou, H.-X., & Pang, X. (2018). Electrostatic interactions in protein structure, folding, binding, and condensation. *Chemical Reviews, 118*(4), 1691–1741.
Zudaire, E., Gambardella, L., Kurcz, C., & Vermeren, S. (2011). A computational tool for quantitative analysis of vascular networks. *PLoS One, 6*(11), Article e27385.